Article

Structural Sensitivities in Bimetallic Catalysts for Electrochemical CO2 Reduction Revealed by Ag-Cu Nanodimers

Jianfeng Huang, Mounir Mensi, Emad Oveisi, Valeria Mantella, and Raffaella Buonsanti

J. Am. Chem. Soc., **Just Accepted Manuscript** • DOI: 10.1021/jacs.8b12381 • Publication Date (Web): 18 Jan 2019

Structural Sensitivities in Bimetallic Catalysts for Electrochemical CO_2 Reduction Revealed by Ag-Cu Nanodimers

Jianfeng Huang,[†] Mounir Mensi,[‡] Emad Oveisi,[§] Valeria Mantella,[†] Raffaella Buonsanti*[†]

[†] Laboratory of Nanochemistry for Energy (LNCE), Institute of Chemical Sciences and Engineering (ISIC), École Polytechnique Fédérale de Lausanne, CH-1950 Sion, Switzerland.

[‡] Institute of Chemical Sciences and Engineering (ISIC), École Polytechnique Fédérale de Lausanne, CH-1950 Sion, Switzerland.

[§] Interdisciplinary Center for Electron Microscopy, École Polytechnique Fédérale de Lausanne, CH-1015 Lausanne, Switzerland.

*Correspondence to: raffaella.buonsanti@epfl.ch

ABSTRACT

Understanding the structural and compositional sensitivities of the electrochemical CO_2 reduction reaction (CO_2RR) is fundamentally important for developing highly efficient and selective electrocatalysts. Here, we use Ag/Cu nanocrystals to uncover the key role played by the Ag/Cu interface in promoting CO_2RR. Nanodimers including the two constituent metals as segregated domains sharing a tunable interface are obtained by developing a seeded growth synthesis, wherein pre-formed Ag nanoparticles are used as nucleation seeds for the Cu domain. We find that the type of metal precursor and the strength of the reducing agent play a key role in achieving the desired chemical and structural control. We show that tandem catalysis and electronic effects, both enabled by the addition of Ag to Cu in the form of segregated nanodomain within the same catalyst, synergistically account for an enhancement in the Faradaic efficiency for C_2H_4 by 3.4-fold and in the partial current density for CO_2 reduction by 2-fold compared with the pure Cu counterpart. The insights gained from this work may be beneficial for designing efficient multicomponent catalysts for electrochemical CO_2 reduction.

INTRODUCTION

Electrochemical CO_2 reduction is an emerging research area due to its potential of converting greenhouse gas CO_2 into useful feedstocks and fuels while storing intermittent renewable energy.[1-2] Among the various CO_2 reduction products, $C_{\geq 2}$ hydrocarbons (e.g., C_2H_4, C_2H_5OH) have attracted much attention because of their higher energy densities compared with C_1 products (e.g., CO, formate, CH_4).[3-4] While high conversion efficiencies have been achieved via device engineering,[5] more fundamental understanding is required for rationally designing CO_2 reduction catalysts with enhanced intrinsic activity and selectivity.

Cu is the most promising monometallic catalyst for electroreducing CO_2 to multicarbon products, albeit it does not possess optimal levels of activity and selectivity.[6] A surge of interest has therefore appeared in modifying Cu catalysts via judiciously manipulating its physicochemical properties,[7] such as sizes,[8] shapes,[9-13] chemical states,[14-17] grain boundaries,[18] stabilities,[19-20] to gain insights into the effect of these parameters on the catalytic behavior and thereby ideally to improve the catalyst performance. More recently, the addition of a second metal to Cu was suggested as another useful means to tune the Cu selectivity and reactivity through tailoring the binding strength and/or binding configuration of intermediates on the catalytic surfaces.[21-29] Enhancements in the electrochemical CO_2 reduction reaction (CO_2RR) have been observed on various Cu-based alloys, including enhanced production of CO on CuAu,[21-22] CH_4 on CuPd,[23] and C_2H_5OH on CuZn.[24] Ag has been shown to substantially activate Cu towards the formation of multicarbon products by mechanisms of either tandem catalysis, in the case of macroscopically phase segregated domains, or strain induced suppression of hydrogen evolution reaction (HER), in the case of surface alloys.[25-28]

The results obtained from Cu-based bimetallic catalysts evidence that neighboring Cu atom ensembles are pivotal to the C-C coupling that is the key step to $C_{\geq 2}$ products.[29] However, to date, most of the aforementioned bimetallic catalysts have been limited to alloys or to systems

without either adequate preservation of Cu ensembles or control on the ensemble size. Thus, it can be anticipated that the study of metallic nanodimers that combine the incorporation of a second metal while preserving the Cu ensemble would be highly relevant to CO_2RR and particularly beneficial to the fundamental understanding of the conversion of CO_2 to C_2 products.

Having this in mind, the challenge becomes the synthesis of such structures. Indeed, while the ability to tailor make bimetallic nanoparticles (NPs) in a wide range of compositions and geometries is of the uttermost importance to tune their optical and catalytic properties, their synthesis in a controlled fashion is still challenging because of the lack of design principles which allow to access the desired structures in a predictive manner.[30-37]

Here, we synthesize Ag-Cu nanodimers (NDs) with tunable domain size by developing a seeded-growth approach through colloidal chemistry, wherein pre-synthesized Ag NPs act as nucleation seeds for the growth of the Cu domain. We find the rational selection of the metal precursor and the reducing agent to be particularly crucial to attain the metallic NDs and their relative counterparts, i.e. Cu NPs and Ag NPs, in a controlled fashion. As a result of the synthetic tunability, we are able to reveal the role of the segregated Ag and Cu nanodomains and of their shared interface in promoting C_2 products in Ag-Cu NDs, together leading to a 3.4-time enhancement in the Faradaic efficiency (FE) for C_2H_4 and to a 2-time in the CO_2RR partial current density in comparison with the Cu NPs counterpart. The enhancement is the result of tandem catalysis and electronic effect, both induced by the coupling of nanoscale segregated Ag and Cu domains through an interfacial region. The fundamental insights gained from the structure/property relationships will facilitate defining the design principles for superior CO_2RR catalysts including multiple components which is the direction to take to break the existing scaling relationships.[38]

EXPERIMENTAL SECTION

Chemicals. Copper(II) acetate monohydrate ($Cu(OAc)_2 \cdot H_2O$, 99.0%), copper(I) acetate (CuOAc, 97%), silver trifluoroacetate (CF_3COOAg, 99.99%), D-(+)-glucose, (99.5%), hexadecylamine (HDA, 90%), L-Ascorbic acid (99%), sodium ascorbate (99%), toluene (anhydrous, 99.8%), potassium carbonate (K_2CO_3, 99%) and Nafion (5wt.%) were purchased from Sigma. Silver nitrate ($AgNO_3$, 99.9995%) was bought from ABCR. Isopropanol (99.5% anhydrous) was obtained from Fluorochem. All chemicals were used as received without further purification. All aqueous solutions were prepared using deionized (DI) water with a resistivity of 18.2 MΩ·cm.

Materials Synthesis. *Ag NPs Synthesis.* Ag NPs were synthesized by sequentially adding 0.045 g HDA, 3.43 mL H_2O, 1.2 mL $AgNO_3$ (100 mM) and 0.37 mL glucose (1 M) into a 40-mL vial at room temperature. After being magnetically stirred for 5 h, the mixture was heated in an oil bath at 100 °C for 1 h. The vial was then removed from the oil and cooled naturally. The particles were washed with water by centrifugation two times (13300 rpm, 10 min), and then either dried in vacuum and re-dispersed in toluene for CO_2RR or directly re-dispersed in H_2O (9 mL) for seeding growth of Ag-Cu NDs.

Cu NPs Synthesis. Cu NPs were synthesized by sequentially adding 0.15 g HDA, 4.55 mL H_2O, and 0.075 mL $Cu(OAc)_2$ (100 mM) into a 40-mL vial at room temperature. After the mixture was magnetically stirred for 12 h, 0.3 mL ascorbic acid (1 M) was added under stirring, and the resulting mixture was heated in an oil bath at 150 °C for 1h. The vial was then removed from the oil and cooled naturally. The particles were washed with water and collected by centrifugation two times (13300 rpm, 10 min), then dried in vacuum and re-dispersed in toluene for CO_2RR.

Ag-Cu NDs Synthesis. Ag-Cu NDs were synthesized using a seed-mediated method. Three different NDs with varied mass ratios of Cu to Ag, i.e., Ag_1-$Cu_{0.4}$ NDs, Ag_1-$Cu_{1.1}$ NDs, Ag_1-

$Cu_{3.2}$ NDs, corresponding to Cu mass percentage of 28.6%, 52.4% and 76.2%, respectively, were achieved by adjusting the amount of the above-synthesized Ag NPs that were used as seeds and the reaction time. Specifically, 0.3 g HDA, 0.3 mL $Cu(OAc)_2$ (100 mM), 8.9 mL H_2O and a specific amount of Ag NPs in H_2O (Ag_1-$Cu_{3.2}$ NDs: 200 μL; Ag_1-$Cu_{1.1}$ NDs: 200 μL; Ag_1-$Cu_{0.4}$ NDs: 400 μL) were sequentially added into a 40-mL glass vial. The resulting mixtures were kept stirred for 5 h, followed with an addition of 0.6 mL ascorbic acid (1 M) under stirring. Finally, the vials were placed in an oil bath of 150 °C for a certain period of heating time (Ag_1-$Cu_{3.2}$ NDs: 20 min; Ag_1-$Cu_{1.1}$ NDs: 12.5 min; Ag_1-$Cu_{0.4}$ NDs: 8 min). After being washed with water and collected by centrifugation two times (13300 rpm, 10 min), the particles were then dried in vacuum and re-dispersed in toluene for CO_2RR.

Preparation of the Ag+Cu Mixtures. Ag+Cu Mixtures were prepared by physically mixing a specific amount of the above-synthesized Ag NPs and Cu NPs. The ratio of Cu to Ag was determined so to be the same as that in Ag_1-$Cu_{1.1}$ NDs.

Characterization. *Electron Microscopy.* Transmission electron microscopy (TEM) images were acquired on a FEI Tecnai-Spirit at 120 kV. High-resolution TEM (HR-TEM), high-angle annular dark-field scanning TEM (HAADF-STEM) images and X-ray energy dispersive (EDX) elemental maps were acquired on a FEI Tecnai-Osiris at 200 kV. High-resolution HAADF-STEM images were taken on a double Cs-corrected FEI Titan Themis 60-300 operated at 300 kV. Samples were prepared by dropping toluene solution containing the nanoparticles on the surface of carbon-coated gold grids (Ted Pella, Inc.).

UV-vis Spectroscopy. UV-vis extinctions were performed in transmission mode using a Perkin Elmer Lambda 950 Spectrophotometer equipped with deuterium lamp as a light source for ultraviolet and tungsten halide lamp as a light source visible and infrared range, and a PMT with peltier-controlled PbS detector. Samples were prepared by dispersing nanoparticles in DI H_2O.

X-ray Diffractometry (XRD). XRD measurements were conducted on a BRUKER D8 Advance instrument with Cu K_α radiation equipped with Bruker LynxEye one-dimensional energy dispersive detector. Samples were prepared by drop-casting nanoparticles on low background silicon holders.

X-ray Photoelectron Spectroscopy (XPS). XPS data were collected on a PHI VersaProbe II scanning XPS microprobe (Physical Instruments AG, Germany) with a monochromatic Al-Kα X-ray source operating at 24.8 W under ultrahigh vacuum conditions. Particle film samples were prepared by drop-casting nanoparticles on silicon substrates.

Inductively Coupled Plasma Optical Emission Spectrometry (ICP-OES). ICP-OES was performed on Agilent 5100 model to determine the Cu and Ag concentration. 5 standard solutions of Cu and Ag were prepared to obtain the calibration curve used to determine the concentrations of the digested nanocrystal solution. The sample solution was prepared by dissolving the nanocrystals in 70% HNO_3 followed with the addition of a specific amount of DI water until the solution reaches the 2% acid content needed for the analysis.

Electrocatalytic Measurements. *Electrode Preparation.* Glassy carbon plates (2.5 cm × 2.5 cm, Type 2, Alfa Aesar) loaded with electrocatalysts served as the working electrode. Before loading electrocatalysts, glassy carbons were typically polished using 1 μm diamond, followed by a rinse with Milli-Q water, ultrasonication in acetone for 5 min and in hexane for 5 min, and blowing dry with N_2. Typically, working electrodes (cathode electrodes) were prepared by evaporating catalyst inks within a circular area of 1.5 cm^2 on the glassy carbon plates. Catalyst inks were prepared by thoroughly mixing nanoparticles (15 μg) in toluene (25 μL) with Nafion/isopropanol mixture (volume ratio: 1:1, 15 μL). Before measurements, the electrodes were stored in a N_2 glove box. Platinum foil and Ag/AgCl electrode (leak free series, Innovative Instruments, Inc.) were used as the counter electrode and reference electrode, respectively.

CO_2 Electrolysis. Electrocatalytic measurements were performed with a potentiostat (Biologic SP-300) in a custom-built gas-tight three electrode cell. A Selemion anion exchange membrane was used to separate the anodic and cathodic compartments. Each compartment was filled with a CO_2-satureated $KHCO_3$ solution (2 mL, 0.1 M) as an electrolyte. Such a $KHCO_3$ solution was prepared by bubbling a freshly prepared K_2CO_3 solution (0.05 M) with CO_2 for 30 min. The working electrodes were held for 1 h at different constant biases (–0.9 V, –1.0 V, –1.1 V, –1.2 V, –1.3 V, –1.4 V vs Reversible Hydrogen Electrode (RHE)) using chronoamperometry. The solution resistance was determined and compensated using the in-built MIR function of the potentiostat, compensating for 85% of the resistance.

Product Analysis. For gas product analysis, a gas chromatograph (GC, SRI instruments) equipped with a HayeSep D porous polymer column, thermal conductivity detector, and flame ionization detector was used. Ultra-high purity N_2 (99.999%) was used as a carrier gas. The concentration of gaseous products was determined using calibration curves from standard gases. For liquid product analysis, a high-performance liquid chromatography (HPLC) on an UltiMate 3000 instrument from Thermo Scientific was used. During electrolysis, CO_2 was constantly bubbled through the electrolyte to prevent depletion of CO_2 in the electrolyte and to allow continuous analysis of gaseous products via a GC. The CO_2 flow was controlled by a mass flow controller (Bronkhorst) and the flow rate was 5.5 sccm, measured from the exhaust of GC using a flowmeter (Ellutia, 7000 Flowmeter). During electrolysis, the CO_2 with gaseous products was allowed to flow directly into the gas sampling loop of the GC for online gaseous product analysis, which took 10.5 min for each run of analysis. The liquid products were collected from the electrolyte after electrolysis and analyzed by the HPLC. Calculations of FE for gaseous products and liquid products are presented in the supporting information (SI).

RESULTS AND DISCUSSION

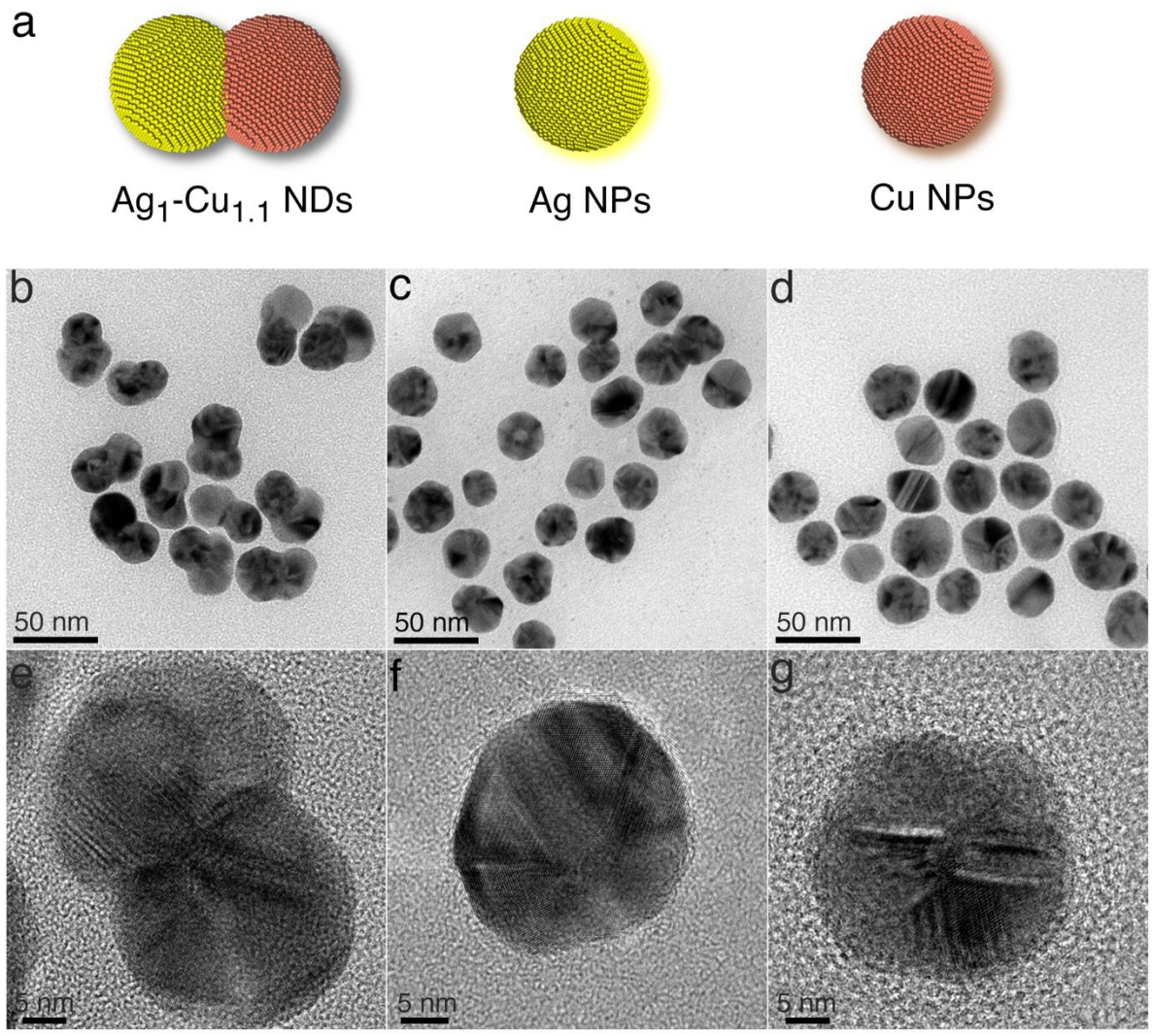

Figure 1. (a) Schematic and (b-g) TEM characterization of the three types of Ag/Cu nanocrystals: TEM and HRTEM images of Ag_1-$Cu_{1.1}$ NDs (b, e), Ag NPs (c, f), Cu NPs (d, g).

The synthesis of the Ag-Cu NDs was achieved by the seeded-growth approach wherein pre-formed ~ 25 nm Ag NPs were used as nucleation seeds for the Cu domains. This technique was chosen for the synthesis because of the demonstrated capability to afford superior compositional and morphological tunability.[37, 39] Briefly, the ligand (HDA), the metal precursor ($Cu(OAc)_2$), the solvent (H_2O) and the seeds (Ag NPs) were sequentially added into a glass vial. After the mixture was stirred for 5 h, the reducing agent (ascorbic acid) was added

under stirring. Finally, the vial was placed in an oil bath of 150 °C for a certain period of time depending on the domain size (details in the Experimental Section).

Figure 1 and 2 report the complete characterization of the synthesized Ag/Cu nanocrystals by various electron microscopy techniques, UV-vis extinction spectra and XRD. From TEM of the Ag-Cu NDs (**Figure 1b)**, uniform calabash-like nanostructures are observed with two discrete spherical domains of distinct contrasts. Each domain is within the size range of 25-30 nm. HRTEM image (**Figure 1e**) shows a clear interface between the two domains, which are both multiply-twinned.[40] HAADF-STEM (**Figure 2a**), which is sensitive to the atomic number of the specimen, confirms the presence of two domains containing different elements (i.e., Ag appears brighter than Cu), in the same nanocrystal. The corresponding EDX maps reveals a segregated distribution of Ag and Cu, suggesting that the higher- and lower-contrast domains are comprised of Ag and Cu, respectively. ICP-OES reports the mass ratio of Cu to Ag to be 1.1, consistent with the similar size of the two domains. This dimer is hereafter denoted as Ag_1-$Cu_{1.1}$ NDs. As control samples, spherical Ag NPs (**Figure 1c, f and Figure 2b**) and Cu NPs (**Figure 1d, g and Figure 2c**) that have a similar size (25-30 nm) to the domains in the Ag_1-$Cu_{1.1}$ NDs and contain multiple nanotwins (crystallite size around 10-15 nm) were also successfully produced, as demonstrated by the same electron microscopy techniques (TEM, STEM, EDX) as those applied for Ag_1-$Cu_{1.1}$ NDs. Consistent with the insights from the electron microscopy, the XRD pattern (**Figure 2d**) of the Ag_1-$Cu_{1.1}$ NDs show two distinct sets of diffraction peaks arising from the fcc structure of Ag and Cu, indicative of the formation of segregated pure metallic Cu and Ag phase in the dimer nanocrystals and discarding the idea of a AgCu alloy. Furthermore, the crystallite size for Cu and of Ag is found to be ~15 nm and ~12 nm, respectively, consistent with the TEM observation that the particles are multiply-twinned. The unique structural features of the NDs are reflected in their optical properties as well. As shown in the UV-visible spectra (**Figure 2e**), the bimetallic Ag_1-$Cu_{1.1}$ NDs exhibit two peaks

at ~ 403 nm and ~ 580 nm, which blue-shifts by ~11 nm and red-shifts by ~ 7 nm with respect to the single characteristic surface plasmon resonance (SPR) peak of monometallic Ag NPs (~ 414 nm) and Cu NPs (~ 573 nm), respectively. Since the size and shape of Ag nanoparticles remain unchanged during the seeded-growth of Ag_1-$Cu_{1.1}$ NDs, the blue shift of the SPR peak experienced by the Ag domains might indicate a charge transfer between Cu domains and Ag domains, as will further be discussed later. All together the characterization results in **Figures 1 and 2** confirm that we successfully synthesized monodispersed Ag/Cu nanocrystals with a tunable structure between the bimetallic Ag-Cu NDs and the monometallic Cu NPs and Ag NPs.

Such an exquisite manipulation of the nanocrystal synthesis was not trivial. Previously, Ag-Cu NDs were synthesized using one-pot synthesis method.[41] However, the method yielded large dimers (> 100 nm) of varied sizes and shapes; also it was unsuccessful to produce NP counterparts of similar physicochemical properties as reference materials. More recently, galvanic exchange between Cu NPs and Ag salts has been employed to synthesize Ag-Cu nanocrescents.[42] Nevertheless, as the Ag nanocrescents grow, the Cu NPs tend to be encapsulated in Ag shells to form a core-shell structure. By contrast, the seeded-growth method employed in this work, being based on the overgrowth of Cu on pre-synthesized Ag NPs, has the great advantages in controlling both the size and structure of the dimer particles. A fine tuning and optimization of the synthetic parameters, including the reducing agent, reaction temperature and time, metal precursors, amount of ligands (**Figures S1-S3)**, was necessary to attain the desired structures. Particularly, we found ascorbic acid to be the reducing agent with an adequate reducing power. Weaker reducing agents, such as glucose, were unable to reduce Cu^{II} ions completely, which resulted in the formation of big Cu_2O particles. Increasing the oxidizing ability of Cu precursor by using copper(I) acetate (CuOAc) still produced similar large Cu_2O particles. Elevating the temperature was not used to enhance the reducing power of

the glucose, as higher temperature than 150 °C often caused a breakage of the vial cap. Stronger reducing agents, such as sodium ascorbate, by contrast, induced a fast nucleation and as a result generated very small particles. In addition, it is noteworthy that the utilization of $Cu(OAc)_2$, instead of $CuCl_2$ which was commonly used in the literature,[41, 43-44] as the Cu precursor, is essential for a successful seeded growth involving Ag NPs as seeds, because the anion Cl^- would etch Ag NPs in the presence of oxygen particularly at high temperature.

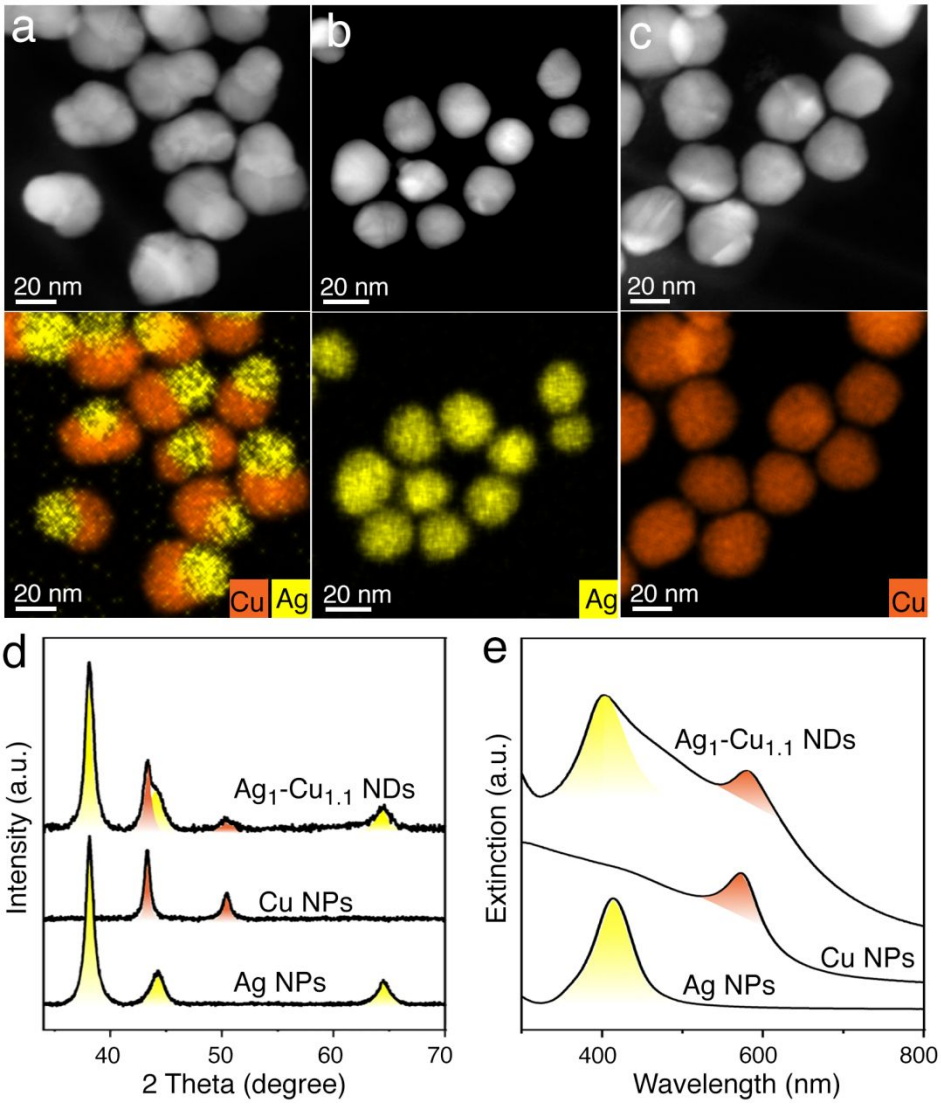

Figure 2. (a-c) HAADF-STEM images of Ag_1-$Cu_{1.1}$ NDs (a), Ag NPs (b), Cu NPs (c), and corresponding EDX elemental maps of Cu (orange) and Ag (yellow). (d, e) XRD patterns (d) and UV-vis spectra (e) of the three types of Ag/Cu nanocrystals.

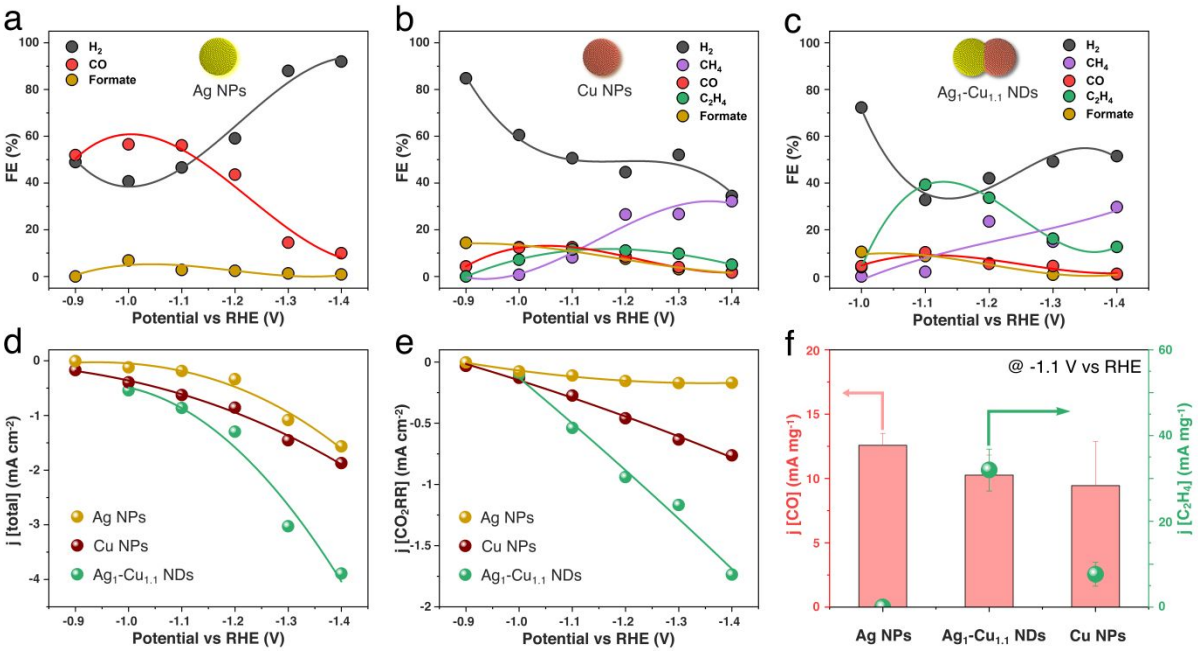

Figure 3. (a-c) FEs for each gaseous product (i.e., H_2, CO, CH_4, C_2H_4) and for the main liquid product (i.e., formate) over (a) Ag NPs, (b) Cu NPs, and (c) Ag_1-$Cu_{1.1}$ NDs. Some other minor liquid products (e.g., acetate, ethylene glycol, ethanol and 1-propanol) with FE < 5% were also produced, as reported in **Figure S4**. (d, e) Total current density (d) and partial current density for the electroreduction of CO_2 (e) (normalized by the electrochemically active surface area, ECSA) over Ag NPs, Cu NPs and Ag_1-$Cu_{1.1}$ NDs. (f) CO and C_2H_4 mass activity of Ag NPs, Cu NPs and Ag_1-$Cu_{1.1}$ NDs at -1.1 V vs RHE. The mass activity is based on the overall mass of Ag and Cu. The error bars show standard deviations from at least three independent measurements.

The catalytic activity of nanoparticles is highly dependent on their physicochemical attributes, such as the size, shape, crystalline structure, surface chemistry.[45-46] To identify the effect arising solely from changes in the structure, it is important to maintain other parameters identical. Because of the success to obtain all the Ag/Cu nanocatalysts in a similar reaction environment involving the same binding ligands, we sought to investigate how the unique dimer structure promotes the CO_2RR. In addition to the electrocatalyst itself, the catalytic

performance in CO_2RR are highly susceptible to the operating conditions, such as the composition of the electrolyte and the electrochemical cell design.[47] For example, the use of gas-diffusion layer in the cell and high concentration of KOH as the electrolyte usually give rise to extremely high current densities up to 750 mA cm^{-2},[5] which, however, might impose limited mass transport and thereby masks the intrinsic activity of the electrocatalysts. In this work, we therefore adopted a reported design of liquid cell with adequate mixing of a 0.1 M $KHCO_3$ electrolyte and flat glassy carbon as catalyst support, which yield relatively low geometric current densities.[48] Moreover, we preferred to skip any thermal or chemical treatment for ligand removal to avoid changes to the intrinsic structure.[49] Since the same ligands functionalize the surface of of the Ag and of the Cu in the NPs and in the NDs, we do not expect them to confer different catalytic behaviour to the studied samples.

We first examined the FE for each product, the results of which are presented in **Figure 3a-c** and **Figure S4**. For pure Ag NPs, the CO_2RR product are CO and formate, and the FE for CO reaches a maximum of 50-60% in the potential range of - 0.9 V – -1.1 V (**Figure 3a**). Using Cu NPs as the electrocatalyst increases the number of products and generates more reduced products, such as CH_4, C_2H_4, *etc.*, at the expense of CO. The highest FE for C_2H_4 is around 12% achieved at -1.1 V (**Figure 3b**). These results are consistent with previous reports on pure Cu NPs and Ag NPs.[12, 50-51] Interestingly, when Ag NPs and Cu NPs are combined together in the form of nanodimers, CO is significantly suppressed when compared with Ag NPs, while C_2H_4 is drastically boosted in comparison with Cu NPs at -1.1 V (**Figure 3c**). Such an enhanced FE of ~ 40% for C_2H_4 obtained from the Ag_1-$Cu_{1.1}$ NDs corresponds to a 3.4-fold enhancement over that from Cu NPs, and is even comparable with the performance of state-of-the-art Cu nanocubes wherein the presence of (100) facets drives the selectivity.[12]

We also assessed the catalytic activity of the three types of nanocrystals under identical reaction conditions through the current densities normalized by the electrochemically active

surface area (ECSA, **Figure S5**). As shown in **Figure 3d**, Ag NPs exhibit lower overall activity than Cu NPs. In stark contrast, when Ag is combined with Cu in the form of Ag-Cu NDs, the activity is significantly enhanced over either single component. However, as the overall current density includes also the current contribution from HER, we decomposed it into individual partial current density for H_2 and CO_2RR products separately, to determine which catalyst performs better for CO_2RR. The results were reported in **Figure 3e**, and interestingly, a similar trend was observed for CO_2RR activity, suggesting that the observed increase in overall activity is contributed by the increased CO_2RR activity. As an example, the partial current density at -1.1 V for Ag_1-$Cu_{1.1}$ NDs is also 2 times higher than that for Cu NPs. In addition, the Ag_1-$Cu_{1.1}$ NDs also exhibit a 4.2-fold higher C_2H_4 mass activity than Cu NPs (**Figure 3f**). The mass activity reported in **Figure 3f** has some interesting implications which will be discussed later. Taken together, these results conclude that Ag_1-$Cu_{1.1}$ NDs, when compared with their constituent counterparts, not only enhance the activity towards CO_2RR, but also improve the selectivity for the C_2H_4 product.

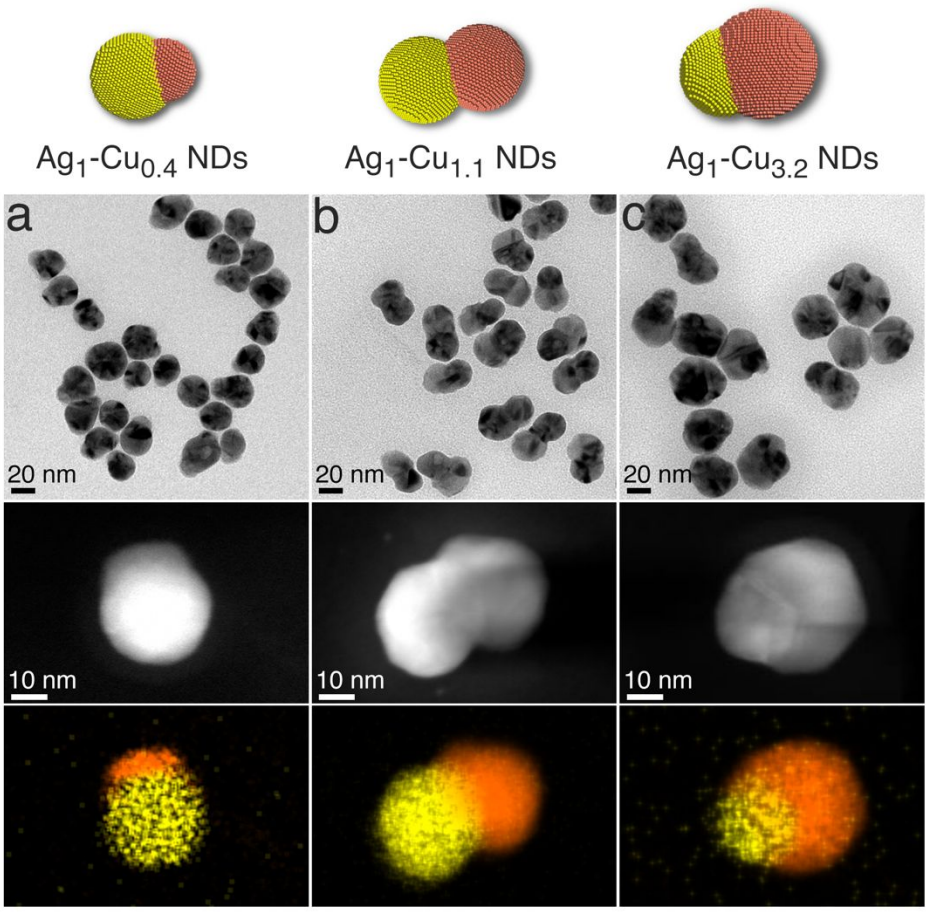

Figure 4. (a-c) Schematic, TEM images, and HAADF-STEM images and combined EDX elemental maps of Cu (orange) and Ag (yellow) of three kinds of Ag-Cu NDs: (a) Ag_1-$Cu_{0.4}$ NDs, (b) Ag_1-$Cu_{1.1}$ NDs, and (c) Ag_1-$Cu_{3.2}$ NDs.

Such a pronounced enhancement in both the selectivity and activity achieved simply by the dimerization of Ag NPs with Cu NPs motivates us to seek out the mechanism by which Ag increases the performance of CO_2RR when interfaced with Cu at the nanoscale. In order to do so, we synthesized NDs with variable size of the Cu domains so to control the extension of the interfacial region (**Figure 4**). We prepared two kinds of dimers, one with smaller Cu size and thus smaller interfacial area (i.e., Ag_1-$Cu_{0.4}$ NDs: **Figure 4a**) and one with bigger Cu size and thus larger interfacial area (i.e., Ag_1-$Cu_{3.2}$ NDs: **Figure 4c**) compared to the original Ag_1-$Cu_{1.1}$ NDs (**Figure 4b**).

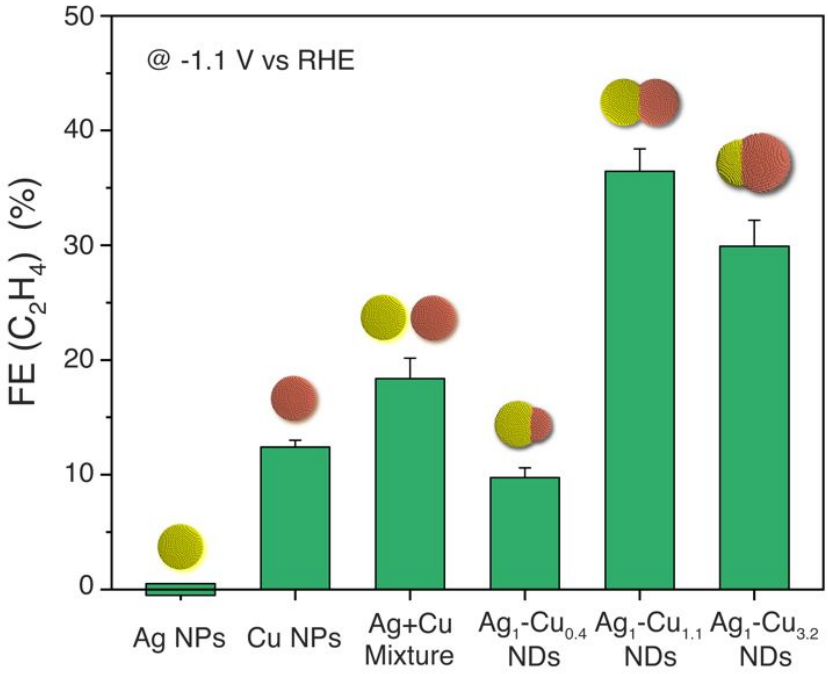

Figure 5. FE for C_2H_4 obtained on different Ag/Cu nanocrystals, including Ag NPs, Cu NPs, Ag+Cu Mixture, Ag_1-$Cu_{0.4}$ NDs, Ag_1-$Cu_{1.1}$ NDs and Ag_1-$Cu_{3.2}$ NDs at -1.1 V vs RHE. The error bars show standard deviations from at least three independent measurements. The full set of electrochemical data, including product distribution, total current density, partial current density for the CO_2RR, and CO and C_2H_4 mass activity at different potentials, is reported in **Figure S6**.

As suggested by earlier studies, adsorbed CO is a crucial intermediate for the formation of C_2H_4.[52-56] Ag is well known to generate more CO than Cu at a given potential and this is consistent with our results. Therefore, one possibility is that in the NDs the Ag domain supplies a high flux of CO to the adjacent Cu domain, which sequentially transforms CO into C_2H_4 (i.e., tandem catalysis).[25, 57-58] To test this hypothesis, we performed one control experiment in which a physical mixture of Ag NPs and Cu NPs (i.e., Ag+Cu Mixture) was employed as the electrocatalyst. A ~ 1.5-fold FE in the FE for C_2H_4 was observed over that of Cu NPs (**Figure 5**), which validates the contribution of Ag to promoting the formation of C_2H_4 through CO

tandem reaction, yet it does not account for the full improvement. We also verified that the additional enhancement observed for the Ag_1-$Cu_{1.1}$ NDs when compared with the Ag+Cu Mixture is not caused by the Cu domains and Ag domains being in closer proximity to each other, as increasing the areal particle density did not lead to a noticeable increase in the FE for C_2H_4 (**Figure S7**). In addition, when analyzing the CO and C_2H_4 mass activity of the Ag/Cu nanocrystals (**Figure 3f**), while the Ag_1-$Cu_{1.1}$ NDs exhibited much higher production rate of C_2H_4 than Cu NPs, they still showed a comparable CO production rate, further confirming that the tandem transformation of CO is not the only mechanism behind the C_2H_4 enhancement. When testing the NDs with different interfacial areas reported in **Figure 4**, a non-monotonic trend was found with the highest FE for C_2H_4 being achieved over the dimers of similar domain size (i.e., Ag_1-$Cu_{1.1}$ NDs). In the Ag_1-$Cu_{0.4}$ NDs, the combination of a less extended interface and of the smaller Cu domain is accompanied by a reduced ethylene and more predominant CO production (**Figure 5 and Figure S8** for other products). The Ag_1-$Cu_{3.2}$ NDs exhibit a substantial ethylene formation, yet not as high as expected based on the extended interfacial area. Rationally designed control experiments evidenced that this behavior is not related to a reduced contribution of the tandem effect due to the Ag domain being smaller than the Cu domain (**Figure S9**). Overall, the results reported in **Figure 5** confirm the importance of the interface in dictating the FE for C_2H_4 but also suggest the existence of a delicate balance between the tandem effect and the extension of the interface.

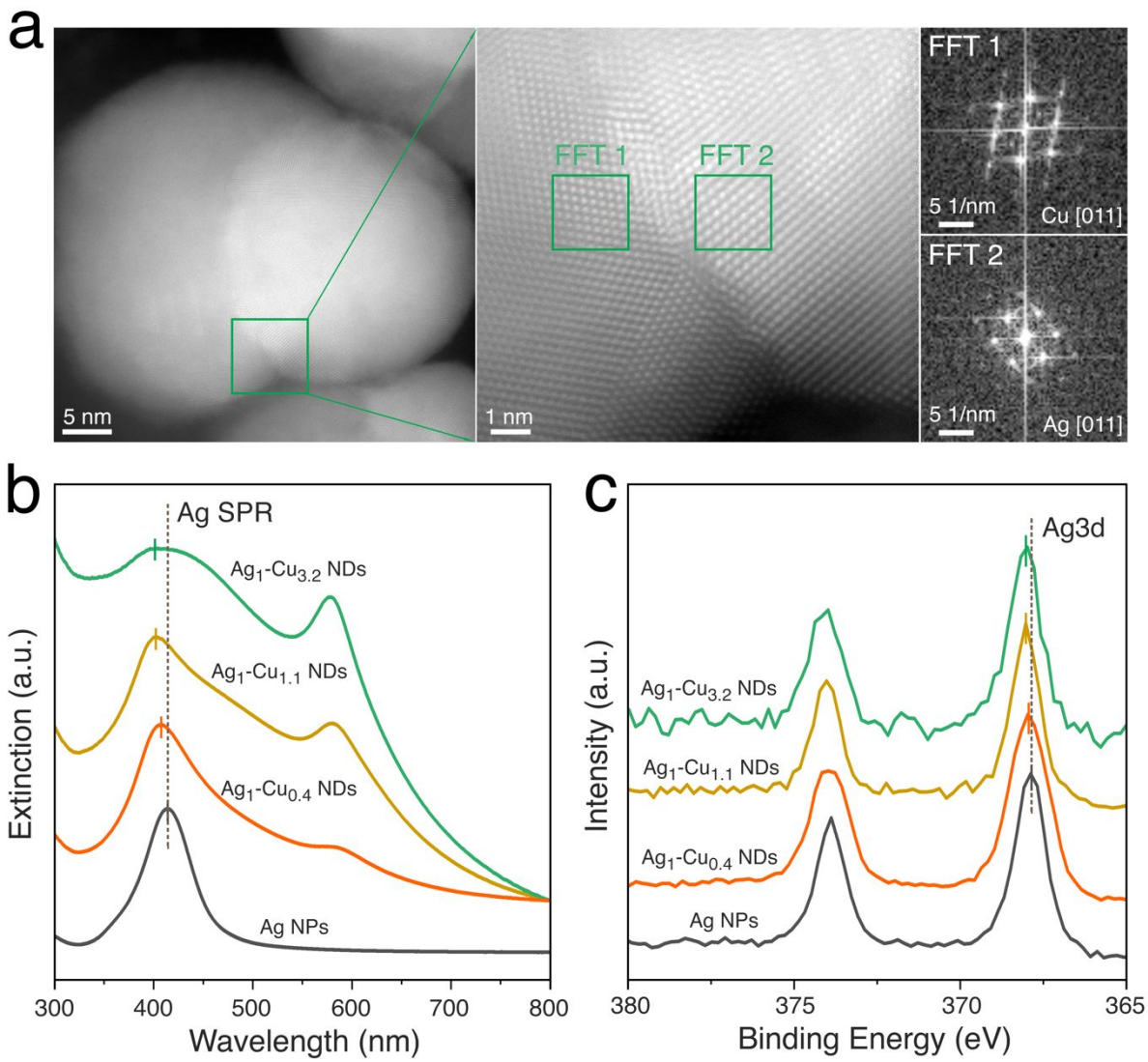

Figure 6. (a) High-resolution HAADF-STEM of the interface, including FFTs. (b) UV-vis spectra and (c) XPS spectra of Ag/Cu nanocrystals.

Previously, HER suppression due to compressive strain induced by surface alloying Ag with Cu has been hypothesized to account for the enhanced selectivity for multi-carbon products in bimetallic alloy catalysts.[26] However, in the case of our NDs, compressive strain is unlikely to be present because an abrupt and clean rather than an alloyed interface is observed with very few (if any) Cu and Ag atoms interdiffused at the interface (**Figure 6a** and after electrochemical experiments in **Figure S10**). The Fast Fourier Transform (FFT) analysis in the interfacial region confirms the presence of segregated Cu and Ag (**Figure 6a**). Consistently,

we did not see a shift in the position of the primary reflections of Cu or Ag from the XRD pattern (**Figure 2d**), which would be expected for strained domains. Interestingly, as mentioned above, we observed a blue shift of the SPR peak of Ag in the Ag_1-$Cu_{1.1}$ NDs relative to the SPR peak of Ag in the Ag NPs (**Figure 2e**), and such a shift increases with the Cu-Ag interfacial area (**Figure 6b**). This blue shift of the SPR peak can be ascribed to the increased electron density in the Ag domain of the dimer, as other parameters (size, shape, dielectric environment, etc.), which affect the SPR position, are all constant. In addition, it is noteworthy that the increased extinction at around 450 nm is caused by the interband transition of metallic Cu, rather than the formation of an Ag/Cu alloy interface (**Figure S11**). Therefore, we can deduce that in the NDs the Ag domain serves as electron acceptor of Cu domain, a phenomenon that is possible only if there is a shared interface and it is not possible in the physical mixture. In fact, since Cu has a higher electron chemical potential than Ag, such an electron transfer is thermodynamically favorable, which drives the transfer of electrons from Cu to Ag as it has also been demonstrated in other studies.[41, 59-60] To confirm the electron transfer process, we further collected the XPS spectra on Cu NPs, Ag NPs, Ag_1-$Cu_{0.4}$ NDs, Ag_1-$Cu_{1.1}$ NDs, and Ag_1-$Cu_{3.2}$ NDs (**Figure 6c**). As the size of the Cu domain increases, the binding energies of the Ag3d core levels in the Ag-Cu NDs continuously blue-shift and concomitant changes are observed also in the XPS and Auger spectra of the Cu (**Figure S12**), which unambiguously verifies the electron transfer from the Cu domain to the Ag domain. Such a phenomenon allows to transform a local effect into a global effect and thus to impact the catalytic behavior of the whole Cu domain when interfaced with the Ag domain by enhancing its intrinsic activity towards C_2H_4. Electron-depleted copper has been already shown to increase the binding of CO on catalyst surface, which in turn facilitates the coupling of CO into C_2H_4.[61] Furthermore, it has been found that there is an optimum in the electron density of copper which maximizes ethylene production.[61] In our NDs, the extent of the interface through the size of the copper

domain allows to modulate the partial copper oxidation state and thus to reach the optimal conditions (interface + copper domain size) to promote CO-CO dimerization. This explains the interface-dependent FE observed on the three different dimers with the maximum C_2H_4 production reached for the Ag_1-$Cu_{1.1}$ NDs (**Figure 5**). In the future, the synthesis of bimetallic heterostructures where the extent of the interface can be varied while preserving the optimal domain size (e.g. by changing the center-to-center distance in NDs) can be targeted to further explore the interface effect now revealed.

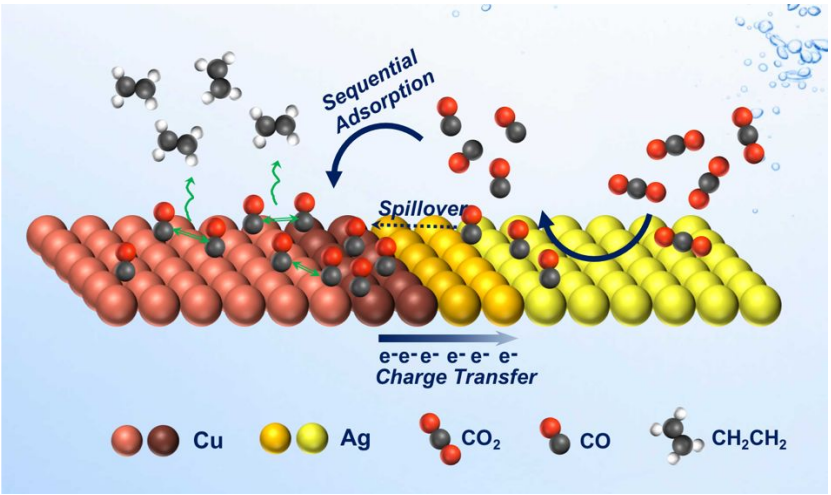

Figure 7. Schematic representation of the proposed mechanism of C_2H_4 promotion in the Ag-Cu NDs which couples the tandem catalysis (CO spillover or sequential adsorption), induced by the presence of Ag and Cu as segregated domains, and the electronic effect caused by the charge transfer at the interface which intimately binds them.

CONCLUSION

In summary, we have developed a novel seeded-growth colloidal approach to tailor make Ag-Cu NDs with different Cu domain sizes (Ag_1-$Cu_{0.4}$, Ag_1-$Cu_{1.1}$ and Ag_1-$Cu_{3.2}$), and achieved a synthetic control over the respective counterparts, Cu NPs and Ag NPs. As a general lesson on the NP synthesis, the proper selection of the metal precursor and the reducing agent is crucial

to achieve the desired bimetallic nanodimers wherein the presence of an interface accounts for charge transfer phenomena which modify the optoelectronic properties compared with the two isolated metals. The synthetic strategy here reported can potentially be extended to other dimer systems in which the two metals are immiscible in the bulk phase (i.e., do not form alloys), such as Cu-Ru, Cu-Rh, Cu-Ir. For miscible metals, such as Cu-Au, the addition of structure-modulating agents (e.g., thiols) might be needed to promote dimerization.[35, 62] These Ag/Cu nanocrystals served as perfect model catalysts to study the compositional and structural sensitivities of CO_2RR in this bimetallic system. The Ag_1-$Cu_{1.1}$ NDs showed a 3.4-fold FE enhancement towards ethylene and a 2-fold improvement in the overall CO_2RR activity compared with the Cu NPs of the similar size and shape. **Figure 7** depicts a schematic summarizing the proposed mechanism behind the electrocatalytic activity of the Ag-Cu NDs. The tandem catalysis and the modified electronic structure, both endowed by the unique Ag-Cu dimer structure, were identified to be the factors accounting for the enhancement in the selectivity for C_2H_4 and activity for CO_2 reduction. Our conclusion suggests that the selectivity of bimetallic catalysts in CO_2RR is sensitive to the lengthscale at which the metals mix. Sequential catalysis and electronic effects were identified as predominant mechanisms behind the increased selectivity towards multicarbon products in Ag/Cu catalysts when Ag and Cu were microscopically segregated (micron scale) and surface alloyed (atomic scale), respectively.[26, 57] Our study on the Ag-Cu nanodimers evidences the combination of the two effects when the mixing of the two metals occurs at the nanoscale. Considering the huge library of materials accessible by colloidal approaches, we believe similar studies have the potential to have a great impact in the development of catalyst design for CO_2RR.

ASSOCIATED CONTENT

Supporting Information. Information related to synthesis, additional CO_2RR results and discussion, optical properties and chemical states of samples. This material is available free of charge via the Internet at http://pubs.acs.org.

ACKNOWLEDGEMENT

This work was supported by the European Research Council under Starting Grant ERC-HYCAT with agreement number 715634 and by the Sandoz Family Foundation.

REFERENCES

1. Seh, Z. W.; Kibsgaard, J.; Dickens, C. F.; Chorkendorff, I.; Norskov, J. K.; Jaramillo, T. F. Combining theory and experiment in electrocatalysis: Insights into materials design. *Science* **2017**, *355*, eaad4998, DOI: 10.1126/science.aad4998
2. Montoya, J. H.; Seitz, L. C.; Chakthranont, P.; Vojvodic, A.; Jaramillo, T. F.; Norskov, J. K. Materials for solar fuels and chemicals. *Nat. Mater.* **2016**, *16*, 70-81, DOI: 10.1038/nmat4778
3. Lim, X. How to make the most of carbon dioxide. *Nature* **2015**, *526*, 628-630, DOI: 10.1038/526628a
4. Bushuyev, O. S.; De Luna, P.; Dinh, C. T.; Tao, L.; Saur, G.; van de Lagemaat, J.; Kelley, S. O.; Sargent, E. H. What Should We Make with CO2 and How Can We Make It? *Joule* **2018**, *2*, 825-832, DOI: 10.1016/j.joule.2017.09.003
5. Dinh, C. T.; Burdyny, T.; Kibria, M. G.; Seifitokaldani, A.; Gabardo, C. M.; Garcia de Arquer, F. P.; Kiani, A.; Edwards, J. P.; De Luna, P.; Bushuyev, O. S.; Zou, C.; Quintero-Bermudez, R.; Pang, Y.; Sinton, D.; Sargent, E. H. CO2 electroreduction to ethylene via hydroxide-mediated copper catalysis at an abrupt interface. *Science* **2018**, *360*, 783-787, DOI: 10.1126/science.aas9100
6. Peterson, A. A.; Abild-Pedersen, F.; Studt, F.; Rossmeisl, J.; Nørskov, J. K. How copper catalyzes the electroreduction of carbon dioxide into hydrocarbon fuels. *Energy Environ. Sci.* **2010**, *3*, 1311–1315, DOI: 10.1039/c0ee00071j
7. Huang, J.; Buonsanti, R. Colloidal Nanocrystals as Heterogeneous Catalysts for Electrochemical CO2 Conversion. *Chem. Mater.* **2018**, *31*, 13-25, DOI: 10.1021/acs.chemmater.8b04155
8. Reske, R.; Mistry, H.; Behafarid, F.; Roldan Cuenya, B.; Strasser, P. Particle size effects in the catalytic electroreduction of CO(2) on Cu nanoparticles. *J. Am. Chem. Soc.* **2014**, *136*, 6978-6986, DOI: 10.1021/ja500328k

9. Ma, M.; Djanashvili, K.; Smith, W. A. Controllable Hydrocarbon Formation from the Electrochemical Reduction of CO2 over Cu Nanowire Arrays. *Angew. Chem. Int. Ed.* **2016**, *55*, 6680-6684, DOI: 10.1002/anie.201601282
10. Manthiram, K.; Beberwyck, B. J.; Alivisatos, A. P. Enhanced electrochemical methanation of carbon dioxide with a dispersible nanoscale copper catalyst. *J. Am. Chem. Soc.* **2014**, *136*, 13319-13325, DOI: 10.1021/ja5065284
11. Roberts, F. S.; Kuhl, K. P.; Nilsson, A. High selectivity for ethylene from carbon dioxide reduction over copper nanocube electrocatalysts. *Angew. Chem. Int. Ed.* **2015**, *54*, 5179-5182, DOI: 10.1002/anie.201412214
12. Loiudice, A.; Lobaccaro, P.; Kamali, E. A.; Thao, T.; Huang, B. H.; Ager, J. W.; Buonsanti, R. Tailoring Copper Nanocrystals towards C2 Products in Electrochemical CO2 Reduction. *Angew. Chem. Int. Ed.* **2016**, *55*, 5789-5792, DOI: 10.1002/anie.201601582
13. Li, Y.; Cui, F.; Ross, M. B.; Kim, D.; Sun, Y.; Yang, P. Structure-Sensitive CO2 Electroreduction to Hydrocarbons on Ultrathin 5-fold Twinned Copper Nanowires. *Nano Lett.* **2017**, *17*, 1312-1317, DOI: 10.1021/acs.nanolett.6b05287
14. Xiao, H.; Goddard, W. A., 3rd; Cheng, T.; Liu, Y. Cu metal embedded in oxidized matrix catalyst to promote CO2 activation and CO dimerization for electrochemical reduction of CO2. *Proc. Natl. Acad. Sci.* **2017**, *114*, 6685-6688, DOI: 10.1073/pnas.1702405114
15. Mistry, H.; Varela, A. S.; Bonifacio, C. S.; Zegkinoglou, I.; Sinev, I.; Choi, Y. W.; Kisslinger, K.; Stach, E. A.; Yang, J. C.; Strasser, P.; Cuenya, B. R. Highly selective plasma-activated copper catalysts for carbon dioxide reduction to ethylene. *Nat. Commun.* **2016**, *7*, 12123, DOI: 10.1038/ncomms12123
16. Ren, D.; Deng, Y. L.; Handoko, A. D.; Chen, C. S.; Malkhandi, S.; Yeo, B. S. Selective Electrochemical Reduction of Carbon Dioxide to Ethylene and Ethanol on Copper(I) Oxide Catalysts. *ACS Catal.* **2015**, *5*, 2814-2821, DOI: 10.1021/cs502128q
17. De Luna, P.; Quintero-Bermudez, R.; Dinh, C.-T.; Ross, M. B.; Bushuyev, O. S.; Todorović, P.; Regier, T.; Kelley, S. O.; Yang, P.; Sargent, E. H. Catalyst electro-redeposition controls morphology and oxidation state for selective carbon dioxide reduction. *Nat. Catal.* **2018**, *1*, 103-110, DOI: 10.1038/s41929-017-0018-9
18. Feng, X.; Jiang, K.; Fan, S.; Kanan, M. W. A Direct Grain-Boundary-Activity Correlation for CO Electroreduction on Cu Nanoparticles. *ACS Cent. Sci.* **2016**, *2*, 169-174, DOI: 10.1021/acscentsci.6b00022
19. Grosse, P.; Gao, D.; Scholten, F.; Sinev, I.; Mistry, H.; Roldan Cuenya, B. Dynamic Changes in the Structure, Chemical State and Catalytic Selectivity of Cu Nanocubes during CO2 Electroreduction: Size and Support Effects. *Angew. Chem. Int. Ed.* **2018**, *57*, 6192-6197, DOI: 10.1002/anie.201802083
20. Huang, J.; Hörmann, N.; Oveisi, E.; Loiudice, A.; De Gregorio, G. L.; Andreussi, O.; Marzari, N.; Buonsanti, R. Potential-induced nanoclustering of metallic catalysts during electrochemical CO2 reduction. *Nat. Commun.* **2018**, *9*, 3117, DOI: 10.1038/s41467-018-05544-3
21. Kim, D.; Resasco, J.; Yu, Y.; Asiri, A. M.; Yang, P. Synergistic geometric and electronic effects for electrochemical reduction of carbon dioxide using gold-copper bimetallic nanoparticles. *Nat. Commun.* **2014**, *5*, 5948, DOI: 10.1038/ncomms5948

22. Kim, D.; Xie, C.; Becknell, N.; Yu, Y.; Karamad, M.; Chan, K.; Crumlin, E. J.; Norskov, J. K.; Yang, P. Electrochemical Activation of CO2 through Atomic Ordering Transformations of AuCu Nanoparticles. *J. Am. Chem. Soc.* **2017**, *139*, 8329-8336, DOI: 10.1021/jacs.7b03516

23. Zhang, S.; Kang, P.; Bakir, M.; Lapides, A. M.; Dares, C. J.; Meyer, T. J. Polymer-supported CuPd nanoalloy as a synergistic catalyst for electrocatalytic reduction of carbon dioxide to methane. *Proc. Natl. Acad. Sci.* **2015**, *112*, 15809-15814, DOI: 10.1073/pnas.1522496112

24. Ren, D.; Ang, B. S.-H.; Yeo, B. S. Tuning the Selectivity of Carbon Dioxide Electroreduction toward Ethanol on Oxide-Derived CuxZn Catalysts. *ACS Catal.* **2016**, *6*, 8239-8247, DOI: 10.1021/acscatal.6b02162

25. Hoang, T. T. H.; Verma, S.; Ma, S.; Fister, T. T.; Timoshenko, J.; Frenkel, A. I.; Kenis, P. J. A.; Gewirth, A. A. Nanoporous Copper-Silver Alloys by Additive-Controlled Electrodeposition for the Selective Electroreduction of CO2 to Ethylene and Ethanol. *J. Am. Chem. Soc.* **2018**, *140*, 5791-5797, DOI: 10.1021/jacs.8b01868

26. Clark, E. L.; Hahn, C.; Jaramillo, T. F.; Bell, A. T. Electrochemical CO2 Reduction over Compressively Strained CuAg Surface Alloys with Enhanced Multi-Carbon Oxygenate Selectivity. *J. Am. Chem. Soc.* **2017**, *139*, 15848-15857, DOI: 10.1021/jacs.7b08607

27. Lee, S.; Park, G.; Lee, J. Importance of Ag–Cu Biphasic Boundaries for Selective Electrochemical Reduction of CO2 to Ethanol. *ACS Catal.* **2017**, *7*, 8594-8604, DOI: 10.1021/acscatal.7b02822

28. Wang, Y.; Wang, D.; Dares, C. J.; Marquard, S. L.; Sheridan, M. V.; Meyer, T. J. CO2 reduction to acetate in mixtures of ultrasmall (Cu) n,(Ag) m bimetallic nanoparticles. *Proc. Natl. Acad. Sci.* **2018**, *115*, 278-283, DOI: 10.1073/pnas.1713962115

29. Ma, S.; Sadakiyo, M.; Heima, M.; Luo, R.; Haasch, R. T.; Gold, J. I.; Yamauchi, M.; Kenis, P. J. Electroreduction of Carbon Dioxide to Hydrocarbons Using Bimetallic Cu-Pd Catalysts with Different Mixing Patterns. *J. Am. Chem. Soc.* **2017**, *139*, 47-50, DOI: 10.1021/jacs.6b10740

30. Gilroy, K. D.; Ruditskiy, A.; Peng, H. C.; Qin, D.; Xia, Y. Bimetallic Nanocrystals: Syntheses, Properties, and Applications. *Chem. Rev.* **2016**, *116*, 10414-72, DOI: 10.1021/acs.chemrev.6b00211

31. Liao, H.; Fisher, A.; Xu, Z. J. Surface Segregation in Bimetallic Nanoparticles: A Critical Issue in Electrocatalyst Engineering. *Small* **2015**, *11*, 3221-46, DOI: 10.1002/smll.201403380

32. Ruditskiy, A.; Peng, H. C.; Xia, Y. Shape-Controlled Metal Nanocrystals for Heterogeneous Catalysis. *Annu. Rev. Chem. Biomol. Eng.* **2016**, *7*, 327-48, DOI: 10.1146/annurev-chembioeng-080615-034503

33. Wang, X.; Ruditskiy, A.; Xia, Y. N. Rational design and synthesis of noble-metal nanoframes for catalytic and photonic applications. *Natl. Sci. Rev.* **2016**, *3*, 520-533, DOI: 10.1093/nsr/nww062

34. Hong, J. W.; Kim, D.; Lee, Y. W.; Kim, M.; Kang, S. W.; Han, S. W. Atomic-distribution-dependent electrocatalytic activity of Au-Pd bimetallic nanocrystals. *Angew. Chem. Int. Ed.* **2011**, *50*, 8876-80, DOI: 10.1002/anie.201102578

35. Feng, Y.; He, J.; Wang, H.; Tay, Y. Y.; Sun, H.; Zhu, L.; Chen, H. An unconventional role of ligand in continuously tuning of metal-metal interfacial strain. *J. Am. Chem. Soc.* **2012**, *134*, 2004-7, DOI: 10.1021/ja211086y

36. Gilroy, K. D.; Yang, X.; Xie, S.; Zhao, M.; Qin, D.; Xia, Y. Shape-Controlled Synthesis of Colloidal Metal Nanocrystals by Replicating the Surface Atomic Structure on the Seed. *Adv. Mater.* **2018**, *30*, e1706312, DOI: 10.1002/adma.201706312

37. Xia, Y.; Gilroy, K. D.; Peng, H. C.; Xia, X. Seed-Mediated Growth of Colloidal Metal Nanocrystals. *Angew. Chem. Int. Ed.* **2017**, *56*, 60-95, DOI: 10.1002/anie.201604731

38. Liu, X.; Xiao, J.; Peng, H.; Hong, X.; Chan, K.; Norskov, J. K. Understanding trends in electrochemical carbon dioxide reduction rates. *Nat. Commun.* **2017**, *8*, 15438, DOI: 10.1038/ncomms15438

39. Casavola, M.; Buonsanti, R.; Caputo, G.; Cozzoli, P. D. Colloidal Strategies for Preparing Oxide-Based Hybrid Nanocrystals. *Eur. J. Inorg. Chem.* **2008**, *2008*, 837-854, DOI: 10.1002/ejic.200701047

40. Marks, L. D.; Howie, A. Multiply-twinned particles in silver catalysts. *Nature* **1979**, *282*, 196-198, DOI: 10.1038/282196a0

41. Huang, X.; Li, Y.; Zhou, H.; Zhong, X.; Duan, X.; Huang, Y. Simplifying the creation of dumbbell-like Cu-Ag nanostructures and their enhanced catalytic activity. *Chem. Eur. J.* **2012**, *18*, 9505-9510, DOI: 10.1002/chem.201200817

42. Osowiecki, W. T.; Ye, X.; Satish, P.; Bustillo, K. C.; Clark, E. L.; Alivisatos, A. P. Tailoring Morphology of Cu-Ag Nanocrescents and Core-Shell Nanocrystals Guided by a Thermodynamic Model. *J. Am. Chem. Soc.* **2018**, *140*, 8569-8577, DOI: 10.1021/jacs.8b04558

43. Jin, M.; He, G.; Zhang, H.; Zeng, J.; Xie, Z.; Xia, Y. Shape-controlled synthesis of copper nanocrystals in an aqueous solution with glucose as a reducing agent and hexadecylamine as a capping agent. *Angew. Chem. Int. Ed.* **2011**, *50*, 10560-4, DOI: 10.1002/anie.201105539

44. He, R.; Wang, Y. C.; Wang, X.; Wang, Z.; Liu, G.; Zhou, W.; Wen, L.; Li, Q.; Wang, X.; Chen, X.; Zeng, J.; Hou, J. G. Facile synthesis of pentacle gold-copper alloy nanocrystals and their plasmonic and catalytic properties. *Nat. Commun.* **2014**, *5*, 4327, DOI: 10.1038/ncomms5327

45. Strasser, P.; Gliech, M.; Kuehl, S.; Moeller, T. Electrochemical processes on solid shaped nanoparticles with defined facets. *Chem. Soc. Rev.* **2018**, *47*, 715-735, DOI: 10.1039/c7cs00759k

46. Kang, Y.; Yang, P.; Markovic, N. M.; Stamenkovic, V. R. Shaping electrocatalysis through tailored nanomaterials. *Nano Today* **2016**, *11*, 587-600, DOI: 10.1016/j.nantod.2016.08.008

47. Clark, E. L.; Resasco, J.; Landers, A.; Lin, J.; Chung, L.-T.; Walton, A.; Hahn, C.; Jaramillo, T. F.; Bell, A. T. Standards and Protocols for Data Acquisition and Reporting for Studies of the Electrochemical Reduction of Carbon Dioxide. *ACS Catal.* **2018**, *8*, 6560-6570, DOI: 10.1021/acscatal.8b01340

48. Lobaccaro, P.; Singh, M. R.; Clark, E. L.; Kwon, Y.; Bell, A. T.; Ager, J. W. Effects of temperature and gas-liquid mass transfer on the operation of small electrochemical cells

for the quantitative evaluation of CO2 reduction electrocatalysts. *Phys. Chem. Chem. Phys.* **2016**, *18*, 26777-26785, DOI: 10.1039/c6cp05287h

49. Kim, D.; Xie, C.; Becknell, N.; Yu, Y.; Karamad, M.; Chan, K.; Crumlin, E. J.; Norskov, J. K.; Yang, P. Electrochemical Activation of CO2 through Atomic Ordering Transformations of AuCu Nanoparticles. *J. Am. Chem. Soc.* **2017**, *139*, 8329-8336, DOI: 10.1021/jacs.7b03516
50. Kim, C.; Jeon, H. S.; Eom, T.; Jee, M. S.; Kim, H.; Friend, C. M.; Min, B. K.; Hwang, Y. J. Achieving Selective and Efficient Electrocatalytic Activity for CO2 Reduction Using Immobilized Silver Nanoparticles. *J. Am. Chem. Soc.* **2015**, *137*, 13844-13850, DOI: 10.1021/jacs.5b06568
51. Liu, S.; Tao, H.; Zeng, L.; Liu, Q.; Xu, Z.; Liu, Q.; Luo, J. L. Shape-Dependent Electrocatalytic Reduction of CO2 to CO on Triangular Silver Nanoplates. *J. Am. Chem. Soc.* **2017**, *139*, 2160-2163, DOI: 10.1021/jacs.6b12103
52. Wuttig, A.; Liu, C.; Peng, Q.; Yaguchi, M.; Hendon, C. H.; Motobayashi, K.; Ye, S.; Osawa, M.; Surendranath, Y. Tracking a Common Surface-Bound Intermediate during CO2-to-Fuels Catalysis. *ACS Cent. Sci.* **2016**, *2*, 522-528, DOI: 10.1021/acscentsci.6b00155
53. Kortlever, R.; Shen, J.; Schouten, K. J.; Calle-Vallejo, F.; Koper, M. T. Catalysts and Reaction Pathways for the Electrochemical Reduction of Carbon Dioxide. *J. Phys. Chem. Lett.* **2015**, *6*, 4073-4082, DOI: 10.1021/acs.jpclett.5b01559
54. Schreier, M.; Yoon, Y.; Jackson, M. N.; Surendranath, Y. Competition between H and CO for Active Sites Governs Copper-Mediated Electrosynthesis of Hydrocarbon Fuels. *Angew. Chem. Int. Ed.* **2018**, *57*, 10221-10225, DOI: 10.1002/anie.201806051
55. Garza, A. J.; Bell, A. T.; Head-Gordon, M. Mechanism of CO2 Reduction at Copper Surfaces: Pathways to C2 Products. *ACS Catal.* **2018**, *8*, 1490-1499, DOI: 10.1021/acscatal.7b03477
56. Montoya, J. H.; Shi, C.; Chan, K.; Norskov, J. K. Theoretical Insights into a CO Dimerization Mechanism in CO2 Electroreduction. *J. Phys. Chem. Lett.* **2015**, *6*, 2032-2037, DOI: 10.1021/acs.jpclett.5b00722
57. Lum, Y.; Ager, J. W. Sequential catalysis controls selectivity in electrochemical CO2 reduction on Cu. *Energy Environ. Sci.* **2018**, *11*, 2935-2944, DOI: 10.1039/c8ee01501e
58. Morales-Guio, C. G.; Cave, E. R.; Nitopi, S. A.; Feaster, J. T.; Wang, L.; Kuhl, K. P.; Jackson, A.; Johnson, N. C.; Abram, D. N.; Hatsukade, T.; Hahn, C.; Jaramillo, T. F. Improved CO2 reduction activity towards C2+ alcohols on a tandem gold on copper electrocatalyst. *Nat. Catal.* **2018**, *1*, 764-771, DOI: 10.1038/s41929-018-0139-9
59. Kim, N. R.; Shin, K.; Jung, I.; Shim, M.; Lee, H. M. Ag–Cu Bimetallic Nanoparticles with Enhanced Resistance to Oxidation: A Combined Experimental and Theoretical Study. *J. Phys. Chem. C* **2014**, *118*, 26324-26331, DOI: 10.1021/jp506069c
60. Chen, Z.; Mochizuki, D.; Maitani, M. M.; Wada, Y. Facile synthesis of bimetallic Cu-Ag nanoparticles under microwave irradiation and their oxidation resistance. *Nanotechnology* **2013**, *24*, 265602, DOI: 10.1088/0957-4484/24/26/265602
61. Zhou, Y.; Che, F.; Liu, M.; Zou, C.; Liang, Z.; De Luna, P.; Yuan, H.; Li, J.; Wang, Z.; Xie, H.; Li, H.; Chen, P.; Bladt, E.; Quintero-Bermudez, R.; Sham, T. K.; Bals, S.; Hofkens, J.; Sinton, D.; Chen, G.; Sargent, E. H. Dopant-induced electron localization drives CO2

reduction to C2 hydrocarbons. *Nat. Chem.* **2018**, *10*, 974-980, DOI: 10.1038/s41557-018-0092-x

62. Huang, J.; Zhu, Y.; Liu, C.; Shi, Z.; Fratalocchi, A.; Han, Y. Unravelling Thiol's Role in Directing Asymmetric Growth of Au Nanorod-Au Nanoparticle Dimers. *Nano Lett.* **2016**, *16*, 617-23, DOI: 10.1021/acs.nanolett.5b04329

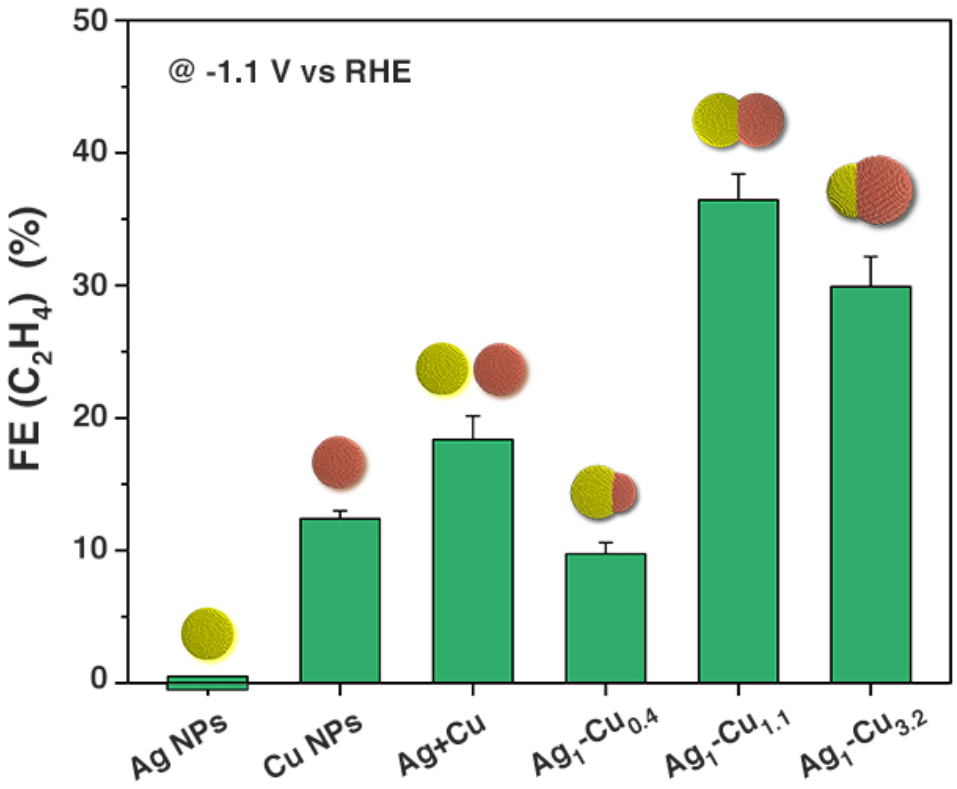

53x44mm (300 x 300 DPI)